

Development of the normalization method for the first large field-of-view plastic-based PET Modular scanner

A. Coussat^{1,2*}, W. Krzemien^{3*}, J. Baran^{1,2}, S. Parzych^{1,2},
E. Beyene^{1,2}, N. Chug^{1,2}, C. Curceanu⁴, E. Czerwiński^{1,2},
M. Das^{1,2}, K. Dulski^{1,2}, K.V. Eliyan^{1,2}, B. Jasińska⁵,
K. Kacprzak^{1,2}, Ł. Kapłon^{1,2}, K. Klimaszewski⁶, G. Korcył^{1,2},
T. Kozik^{1,2}, K. Kubat^{1,2}, D. Kumar^{1,2}, A. Kunimal Vendan^{1,2},
E. Lisowski⁷, F. Lisowski⁷, J. Mędrala-Sowa^{1,2}, S. Moyo^{1,2},
W. Mryka^{1,2}, S. Niedźwiecki^{1,2}, P. Pandey^{1,2}, E. Perez del Rio^{1,2},
L. Raczyński⁶, M. Rädler^{1,2}, S. Sharma^{1,2}, M. Skurzok^{1,2},
E.Ł. Stępień^{1,2}, K. Tayefi^{1,2}, P. Tanty^{1,2}, W. Wiślicki⁶,
P. Moskal^{1,2}

¹Faculty of Physics, Astronomy and Applied Computer Science,
Jagiellonian University, Łojasiewicza 11, Kraków, Poland.

²Center for Theranostics, Jagiellonian University, Kopernika 40, Kraków,
Poland.

³High Energy Physics Division, National Centre for Nuclear Research,
Andrzeja Sołtana 7, Otwock-Świerk, Poland.

⁴INFN, Laboratori Nazionali di Frascati, Via E. Fermi 40, 00044,
Frascati, Italy.

⁵Institute of Physics, Maria Curie-Skłodowska University,
Radziszewskiego 10, 20-031, Lublin, Poland.

⁶Department of Complex Systems, National Centre for Nuclear Research,
Andrzeja Sołtana 7, Otwock-Świerk, Poland.

⁷Cracow University of Technology, Warszawska 24, 31-864, Kraków,
Poland.

*Corresponding author(s). E-mail(s): aurelien.coussat@uj.edu.pl;
wojciech.krzemien@ncbj.gov.pl;

Abstract

Background

In positron emission tomography acquisition, sensitivity along a line-of-response can vary due to crystal geometrical arrangements in the scanner and/or detector inefficiencies, leading to severe artefacts in the reconstructed image. To mitigate these effects, data must be corrected by a set of normalization coefficients applied to each line of response.

The J-PET Modular scanner is a positron emission tomograph made of 50 cm long plastic strips arranged axially, with signal read-outs from both sides. This design significantly reduces the overall cost of the scanner and is well-suitable for the development of long axial field-of-view and total-body devices. The scanner is assembled from a set of stand-alone detection modules connected to front-end electronics. Each module forms a lightweight, independent unit which can be easily transported and assembled in various configurations. In its default configuration, the modules are arranged cylindrically side-by-side with a pitch of 7.5° , resulting in a radius of about 76.2 cm and an axial field-of-view of 50 cm. The Modular J-PET scanner is currently in operation at the Jagiellonian University in Kraków (Poland).

Methods

We have implemented a normalization method for the large field-of-view plastic-based J-PET Modular scanner using the component-based approach.

We considered a normalization model that incorporates both geometric and detection efficiency factors. We estimated the geometric normalization factors for the J-PET Modular scanner using Monte Carlo simulations. We also analysed the effects of variations in detection efficiency. A dedicated cylindrical phantom was simulated to investigate the impact of various factors on image quality. The image quality was quantified in terms of radial and axial uniformity metrics, and the standard deviation to mean intensity ratio, determined for a set of image slices.

Results

Without normalization, reconstructions of a uniform cylinder exhibit artefacts in the form of a dip located at the centre of the cylinder. In the case of variable detector efficiencies, several more pronounced artefacts appear. These artefacts were satisfactorily compensated using the efficiency normalization factors. The application of geometrical corrections lowers the non-uniformity of the image expressed as a standard deviation-to-mean ratio to a range between 5.5% to 8.5%.

Computationally, the technique is straightforward to parallelize, making it time-efficient. Preliminary estimates of computing times and memory requirements suggest that the method is appropriate for use with long axial field-of-view scanners, such as the Modular J-PET or the total-body J-PET, the latter currently under development at the Jagiellonian University.

Keywords: positron emission tomography, normalization corrections, medical image reconstruction, large field-of-view scanner

1 Introduction

Positron Emission Tomography (PET) is a medical imaging technique that gives access to physiologic information by reconstructing the spatial distribution of radiotracers based on the detection of back-to-back photon pairs emitted from the patient’s body. This method enables non-invasive, three-dimensional imaging in vivo and is commonly used in clinical contexts, particularly for oncological diagnosis and treatment, as well as in studies of brain diseases, cardiology and other medical fields. The introduction of the long axial field-of-view (LAFOV) and total-body (TB) PET modalities open new application perspectives [1, 2] but also new challenges [3, 4].

PET image reconstruction is typically achieved using iterative algorithms that transform the acquired data into an image. Producing high-quality PET images requires incorporating several corrections to compensate for various sources of error and non-uniformity present in the collected data. Among the most important factors are the attenuation corrections, which compensate for the photon absorption in the patient’s body, and the estimation of the additive background terms formed by 1. the registered uncorrelated photon pairs (called *accidental* or *random* coincidences) due to the finite time resolution of the time window used to select the true pairs; 2. the fraction of registered photon pairs in which at least one of the photons is deflected in the patient’s body (called *scatters*). *Normalization* corrections are applied to compensate for the variation in the efficiency of the coincidence detector pairs, which can be caused by factors such as the detection units arrangement and shape, crystal imperfections or front-end electronics effects. Physical effects such as non-collinearity of photon emission pairs or depth-of-interaction variations can be modelled in the data or image domain using techniques like point-spread-function parametrization [5]. The lack of appropriate corrections can degrade the image quality and lead to artefacts, consequently deteriorating the image diagnostic value. In this article, we focus on normalization correction methods.

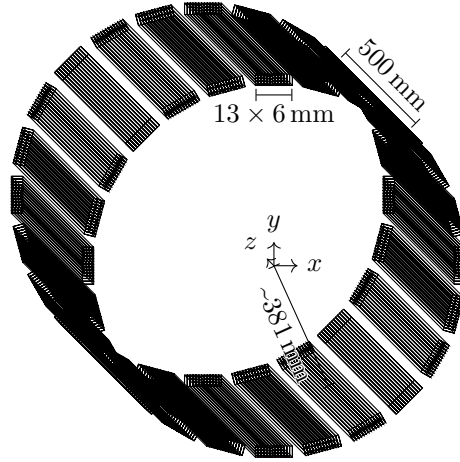
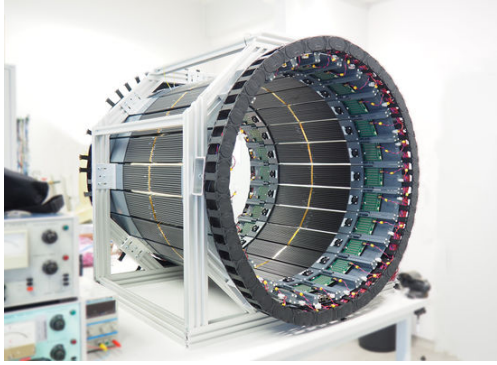
The most popular approach to determine normalization coefficients is the component-based normalization (CBN) method [6–9]. In CBN, the sensitivity variations are modelled as a product of various components estimated separately based on the dedicated scans. Since the introduction of this method, several investigations have been performed to improve the model accuracy by incorporating terms modelling more sophisticated effects. However, the normalization process requires a relatively long scanning time which could otherwise be used for medical purposes. Also, the use of special phantoms made the procedure complicated. Consequently, efforts were made to simplify the normalization acquisition protocol [10]. To mitigate the low variance of the estimates (co)sum-fan algorithms were proposed [11, 12]. In addition, numerous studies tried to optimize the estimation procedures [13–15]. For instance, in CBN models, the components can be classified into time-invariant factors (e.g. geometry-dependent), which in principle can be estimated only once, and time-variant terms (e.g. intrinsic scintillator efficiencies) which must be updated periodically based on regular scans. Studies were conducted to estimate how often such scans need to be repeated for the PET-MR modality [16]. Also, trials of self-normalization techniques were explored [17], where part of the coefficients is derived directly from the routine emission scan eliminating the need for dedicated scans. A separate study was devoted

to the CBN model in the context of event-based motion-correction application [18] and continuous bed motion acquisition [19]. The consensus is that the normalization is an essential step and CBN remains the preferred method for most of the clinical and research PET scanners [20] including the novel generation of LAFOV tomographs like Biograph Vision Quadra [21] and TB Explorer scanners [3, 22]. However, the details of the optimal CBN model are highly dependent on scanner design, crystal types, front-end electronics and other factors.

In this contribution, we concentrate on the CBN method developed for the 50 cm field-of-view (FOV) plastic-based Jagiellonian Positron Emission Tomography (J-PET) Modular scanner [23]. The J-PET technology utilizes long plastic strips arranged axially, with signal read-outs from both sides. This design significantly reduces the overall cost of the scanner and is well-suitable for the development of LAFOV and TB devices. The application of the J-PET scanner is not limited only to medical two-photon tomography [24] but covers a broad range of topics from fundamental physics studies [25–29], simultaneous multi-tracer imaging, proton beam range monitoring [30, 31] and innovative positronium imaging [32, 33]. Detailed information about the potential clinical applications of J-PET technology can be found in Ref. [34].

The Modular J-PET scanner, currently in operation at the Jagiellonian University in Kraków (Poland), was notably used to reconstruct the first positronium image of the human brain in vivo [33]. A depiction of the detector is shown in Fig. 1a. The scanner is assembled from a set of stand-alone detection modules connected to front-end electronics. Each module forms a lightweight, independent unit (of about 2 kg) which can be easily transported and assembled in various configurations. This modular design allows the scanner to be configured as a single layer (with 24 modules) or multiple layers (such as 8 or 16 modules) to meet specific requirements. In addition, modules can be operated individually, allowing the Modular J-PET to be used as a multirole detector. In its default configuration, the modules are arranged cylindrically side-by-side with a pitch of 7.5° , resulting in a radius of about 76.2 cm and an axial FOV of 50 cm. The geometry of the scanner is shown in Fig. 1b. Each module consists of 13 EJ-230 (ELJEN Technology) plastic scintillator strips with dimensions of $24\text{ mm} \times 6\text{ mm} \times 500\text{ mm}$. The annihilation photons passing through the plastic scintillator strips interact predominately via Compton scattering.

In this article, we introduce the CBN model and its implementation adapted to the Modular J-PET. Through Monte Carlo (MC) simulations we demonstrate the relative improvement of the reconstructed images and discuss the stability of the solution. Although this work primarily focuses on the Modular J-PET modality, we plan to extend the procedure to the TB J-PET scanners [35], which presents additional challenges due to their increased length. The article is organized as follows: Section 2.1 introduces the normalization coefficients as a part of the system model and explains their integration into the Maximum-Likelihood Expectation-Maximisation (MLEM) algorithm scheme. The section 2.2 outlines the rationale behind the CBN method. The different terms of the normalization model are explained together with the corresponding equations. Sections 2.4.1 to 2.4.5 provide the details of the performed MC simulations. Sections 2.4.6 and 2.4.7 present the details of image reconstruction settings and the quality metrics, respectively. In Section 3, we present and



(a) Photography of the Modular J-PET scanner. (b) Schematic representation of the Modular J-PET scanner (not to scale).

Fig. 1: Photography and geometry of the Modular J-PET scanner, in its cylindrical set-up, as considered throughout this article.

discuss the distributions of normalization coefficients together with the results of the reference phantom image reconstruction. The article concludes with a summary in Section 4, which also discusses the adaptation of the proposed method to the TB J-PET prototype currently under construction. Additionally, the set of additional checks we performed throughout our study is presented. The article is supplemented with three appendices. The reference analytical model of the sensitivity is introduced in Section A. The description of additional tests of the robustness of the results is given in Section B. Finally, the influence on the results of the projector choice is reported in Section C.

2 Materials and Methods

2.1 Relations between the system model, sensitivity map and normalization components

The objective of PET tomography is to reconstruct the radiotracer activity distribution $f(\mathbf{x})$ based on a measured set of photon coincidences $\mathbf{y} = (y_1, \dots, y_P)$, registered by the scanner consisting of P detector pairs (projections). Typically, a continuous radiotracer distribution is approximated by a sum of discrete basis functions $b_q(\mathbf{x})$, e.g. Q cubic voxels: $f(\mathbf{x}) \approx \sum_{q=1}^Q x_q b_q(\mathbf{x})$ where $\mathbf{x} = (x_1, \dots, x_Q)$ [5]. The statistical model for the measurement is defined as

$$\mathbf{y} = \mathbf{A}\mathbf{x} + \mathbf{b}. \quad (1)$$

The matrix \mathbf{A} represents the system model and the additive component $\mathbf{b} = (b_1, \dots, b_p)$ expresses the mean value of background events e.g. random and scatter coincidences.

The system model \mathbf{A} represents the relationship between the measured data \mathbf{y} in the projection space and the radiotracer activity distribution $f(\mathbf{x})$ in the image space. It can incorporate the geometry of the scanner, physical processes and other effects which are the sources of various uncertainties degrading the reconstructed image quality. In the voxelized version, the system model is a $Q \times P$ matrix, and its elements A_{pq} correspond to the probability that a photon pair originating from the voxel q is registered by the detector pair p .

The final quality of the reconstructed image depends strongly on the accuracy of the system model. The efficient implementation of the system model in the form of a matrix used by the reconstruction algorithm poses a technical challenge. On one hand, the granularity of the matrix should be high enough to provide the required precision of the model. On the other hand, fast access is necessary since in the typical iterative reconstruction process, a series of forward and backward projection steps are performed, in which the system matrix elements are read continuously by the image reconstruction algorithm. This problem becomes even more challenging for large FOV and TB scanners, for which the storage of the full system matrix becomes impossible. Hence, approximate methods must be used, which leads to a compromise between accuracy and efficiency.

Various methods were proposed to estimate the system matrix elements. One can classify them into four categories [5]: 1. MC-simulation-based; 2. analytical methods; 3. direct computation from dedicated normalization measurements; 4. hybrid methods. One of the common approaches is to factorize the system model into sub-matrices corresponding to different effects which are then modelled independently. For instance, decomposition can be done in the following form:

$$\mathbf{A} = \mathbf{A}^{\text{norm}} \mathbf{A}^{\text{scanner}} \mathbf{A}^{\text{res}} \mathbf{A}^{\text{atten}}, \quad (2)$$

where \mathbf{A}^{norm} is a diagonal matrix modelling the inefficiencies in the projection space, $\mathbf{A}^{\text{scanner}}$ incorporates the effects of the scanner geometry, \mathbf{A}^{res} models the resolution degradation due to the detector positron range, acollinearity effect, inter-detector penetration and others, and $\mathbf{A}^{\text{atten}}$ models the attenuation effects of the object. Note that $\mathbf{A}^{\text{scanner}}$ only models the efficiency of the scanner with respect to the position of each detector, without taking into account additional effects that are modelled by \mathbf{A}^{norm} , such as detector density or line of response (LOR) obliqueness. Effects modeled by \mathbf{A}^{norm} are explained more in detail in Section 2.3.

This work concentrates on the estimation of the \mathbf{A}^{norm} matrix components for the J-PET detector. The discussion and the sophisticated method for modelling \mathbf{A}^{res} in the context of the future TB J-PET scanners can be found in [36].

Data acquired is turned into an image using a tomographic image reconstruction technique. For PET imaging, MLEM is the most commonly used reconstruction method. MLEM is an iterative numerical algorithm designed to find the maximum likelihood estimate of the image model given the measured data. It was introduced in the domain of PET image reconstruction by Ref. [37], under the assumption that the

measured data are realizations of Poisson processes. Using the notations introduced above, a MLEM iteration can be defined as:

$$x_q^{(k+1)} = \frac{x_q^{(k)}}{S_q} \sum_{p=1}^P A_{pq} \frac{y_p}{\sum_{q'=1}^Q A_{pq'} x_{q'}^{(k)}} \quad (3)$$

where $x^{(k)}$ is the image estimate at the k^{th} iteration. In the absence of any prior information about the image, the first estimate $x^{(1)}$ is typically set to a uniform image of ones. The sensitivity map \mathbf{S} of the scanner is a distribution in the image space whose elements consist of values proportional to the probabilities of registration of an annihilation pair by any detector unit. Formally, the relation between the sensitivity map and the system matrix can be expressed as a summation over the probabilities of detection for all detector pairs:

$$S_q = \sum_{p=1}^P A_{pq}. \quad (4)$$

The MLEM approach has several advantages, e.g. it naturally incorporates the modelling of noise, and it allows to model the detector influence in the system model \mathbf{A} .

Normalization factors are then incorporated into the MLEM reconstruction procedure: Eq. (3) is updated to become

$$x_q^{(k+1)} = \frac{x_q^{(k)}}{S'_q} \sum_{p=1}^P A_{pq} \frac{y_p}{n_p \sum_{q'=1}^Q A_{pq'} x_{q'}^{(k)}} \quad (5)$$

where S' is the normalized sensitivity map defined by updating Eq. (4) to incorporate normalization factors:

$$S'_q = \sum_{p=1}^P n_p A_{pq}. \quad (6)$$

2.2 Determination of normalization coefficients

The diagonal matrix \mathbf{A}^{norm} models the probabilities of coincidence registration in the projection space indexed by p . The proper determination of the normalization coefficients $n_p = \frac{1}{A_p^{\text{norm}}}$ permits compensating for the detector efficiency variation, and for the geometrical effects not included in the scanner projection model $\mathbf{A}^{\text{scanner}}$.

In principle, the normalization coefficients n_p could be estimated from the direct scan of a phantom with known activity by using the relation

$$N_p^{\text{expected}} = n_p N_p^{\text{registered}}, \quad (7)$$

where $N_p^{\text{registered}}$ is the number of registered coincidences along projection p , and N_p^{expected} is the expected number of emitted coincidences along that same projection

p , calculated based on known activity and the phantom shape. This method is known as direct normalization [20]. However, this approach becomes impractical, especially for large-FOV detectors, due to statistical limitations linked with problems related to the available projection space coverage. For instance, to estimate the normalization coefficients from all the projections with an accuracy of 1% for a scanner with N crystals, one needs to collect roughly $10^4 \times \frac{N(N-1)}{2}$ photon coincidences. In the case of the modular J-PET detector with a number of projections $P \approx 10^8$, one would need to collect approximately 10^{12} coincidences to fulfil this condition. In addition, two problems make this task even more challenging. First, not all projections are equally probable, and some oblique projections have a fairly low registration probability. Second, since the normalization data should contain low random and scatter rates, a low-activity source must be used, which must be compensated by an extremely long normalization scan, rendering the whole procedure impractical.

2.3 Component-based normalization model

To mitigate the aforementioned problems, the so-called component-based normalization (CBN) method was developed. It relies on further factorization of the normalization coefficients into sub-factors that can be estimated separately. The underlying assumption of this approach is that the sub-factors are statistically independent, which in principle is not true, but in practice works reasonably well. To limit the variance of the estimations, the projections which are assumed to have similar properties and grouped, and the corresponding mean values are used in the calculation. All the following definitions are adapted from Pépin et al. [38].

To describe the CBN model we consider the scanner device composed of the detection modules (strips) arranged cylindrically. The detection modules are further divided into virtual crystals. Each projection LOR is indexed by four integers $uivj$. This LOR represents the projection joining detector region ui (the strip i at position u) with detector region vj (the strip j at position v), as illustrated by Fig. 2. Let t_{uivj} denote the number of coincidences along LOR $uivj$.

The component-based normalization factor along the LOR $uivj$ can now be defined by

$$n_{uivj} = b_u^{\text{ax}} \cdot b_v^{\text{ax}} \cdot g_{uv}^{\text{ax}} \cdot g_{ij}^{\text{tr}} \cdot \epsilon_{ui} \cdot \epsilon_{vj} \quad (8)$$

where b^{ax} represents the block profile factors, g^{ax} the axial geometric factors, g^{tr} the transverse geometric factors and ϵ the intrinsic detector efficiencies¹.

Some of these factors are inter-correlated and dependent on each other, that is to calculate one, another one is used. This fact will be highlighted in further equations (Eqs. (11) to (15)). Furthermore, because geometric factors (g^{ax} and g^{tr}) depend only on the detector geometry, they can in principle be purely determined from MC, whereas detector efficiency factors (ϵ) must be determined from a dedicated scan as they can vary due to various effects [16].

¹Some CBN models can include additional factors e.g. transverse interference functions which are meant to compensate for non-uniformity of detection efficiency with respect to the location of a crystal in a detector block. However, this one can be ignored in the context of J-PET because it uses continuous plastic scintillator strips.

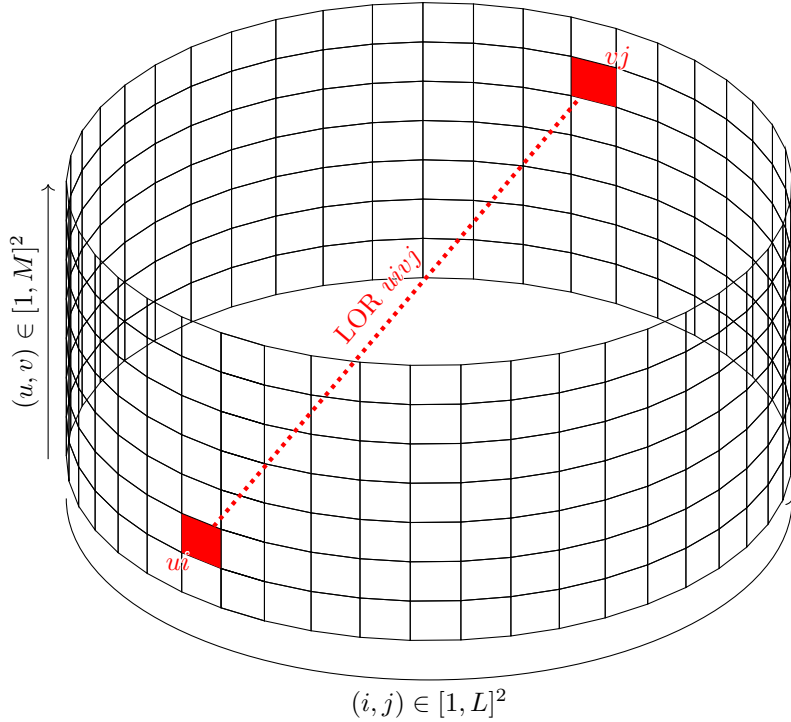


Fig. 2: Projection notation. The axial (z) direction is oriented vertically from the bottom to the top. The scanner is composed of L strips split into M (pseudo-)crystals. The indexes i and j denote the strip, whereas the indexes u and v denote the position along the strip, which corresponds to pseudo-crystal in the context of J-PET's continuous strip technology. This figure was reproduced from Pépin et al. [38].

The block profile factors (b^{ax}) are designed to ensure a uniform hit count across all rings of the scanner. In the case of J-PET, the factors ensure a uniform hit count across all axial bins. They are computed from the LOR sum of all LORs for a single axial direction, i.e. all LORs that lie on a single plane parallel to the xy plane. We denote such a LOR sum for axial position u as $\mathcal{S}_u^{b^{\text{ax}}}$ and define it as

$$\mathcal{S}_u^{b^{\text{ax}}} = \sum_{i=1}^L \sum_{j=1}^L t_{uiuj}. \quad (9)$$

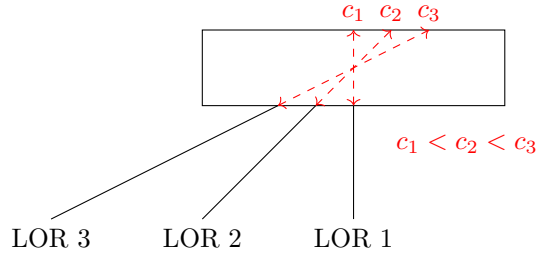
Using the definition of Eq. (9), the block profile factors for the axial position u is now defined as

$$b_u^{\text{ax}} = \sqrt{\frac{\frac{1}{M} \sum_{v=1}^M \mathcal{S}_v^{b^{\text{ax}}}}{\mathcal{S}_u^{b^{\text{ax}}}}}. \quad (10)$$

Geometrical factors (g^{ax} and g^{tr}) compensate for the variation in efficiency induced by the geometrical arrangement of the detector strips.



(a) Exposed detector width variation as a function of the radial position. (b) LOR distance variation as a function of the radial position.



(c) Detection probability variation as a function of the LOR obliqueness. Traversal of more material induces a higher detection probability.

Fig. 3: Geometric effects influencing detection efficiency.

Axial geometric factors account for sensitivity variation caused by the incidence angle of the LOR against the detector strip in the axial direction. The axial geometric factors are therefore a function of the axial distance $|u - v|$. The factors are computed based on the sum of all the LORs connecting the axial position u with the axial position v . We denote such a LOR sum as $\mathcal{S}_{uv}^{g^{ax}}$ and define it as follows

$$\mathcal{S}_{uv}^{g^{ax}} = b_u^{ax} \cdot b_v^{ax} \sum_{i=1}^L \sum_{j=1}^L t_{uivj} \cos \theta \quad (11)$$

where θ is the angle between the LOR and the transverse plane, and b^{ax} are the axial block profile factors defined by Eq. (10). The factor $\cos \theta$ is an activity correction factor, used to compensate for the difference in activity located along each LOR in the axial direction. Using the definition of Eq. (11), the axial geometric factor g^{ax} between two axial positions u and v is defined as the ratio between $\mathcal{S}_{uv}^{g^{ax}}$ and the mean

of $\mathcal{S}_{uv}^{g^{\text{ax}}}$ over all u and v , hence

$$g_{uv}^{\text{ax}} = \frac{1}{M^2} \sum_{u'=1}^M \sum_{v'=1}^M \mathcal{S}_{u'v'}^{g^{\text{ax}}} / \mathcal{S}_{uv}^{g^{\text{ax}}}. \quad (12)$$

Transverse geometric factors also account for sensitivity variation caused by the incidence angle of the LOR against the detector strip, but this time along transverse planes. The LOR efficiencies increase towards the edge of the FOV because LORs form increasingly oblique angles as they approach the edge of the FOV, resulting in longer intersections with the detector strips. However, there are additional effects at play: the exposed detector width (Fig. 3a) and the LOR density (Fig. 3b) decreases as the radial distance increases. The factors are computed from the sums of all the LORs that share the same radial bin inferred from the indices i and j of the LOR. The radial bin is denoted $r \in [1; K]$, where K is the total number of radial bins. The LOR sum is denoted $\mathcal{S}_r^{g^{\text{tr}}}$ and is defined as

$$\mathcal{S}_r^{g^{\text{tr}}} = \sum_{u=1}^M \sum_{v=1}^M \underbrace{\sum_{i=1}^L \sum_{j=1}^L}_{x_r(i,j)=r} c_{uivj} \quad (13)$$

where $x_r(i, j)$ is the radial bin of the LOR connecting strips i and j , and c_{uivj} is the number of coincidence for LOR $uivj$ with the correction given by

$$c_{uivj} = a_{uivj} \cdot b_u^{\text{ax}} \cdot b_v^{\text{ax}} \cdot g_{uv}^{\text{ax}} \cdot t_{uivj} \quad (14)$$

where a_{uivj} is the activity correction factor defined as the inverse of the analytical projection of the source [38]. The factors b^{ax} are given by Eq. (10). The radial binning procedure is designed such that every bin corresponds to the same number of possible LORs and is presented in Fig. 4. Finally, using the definition of Eq. (13), the transverse geometric factor g^{tr} for a radial bin r is defined as the ratio between $\mathcal{S}_r^{g^{\text{tr}}}$ and the mean of $\mathcal{S}_r^{g^{\text{tr}}}$ over all r , hence

$$g_r^{\text{tr}} = \frac{1}{K} \sum_{r'=1}^K \mathcal{S}_{r'}^{g^{\text{tr}}} / \mathcal{S}_r^{g^{\text{tr}}}. \quad (15)$$

Intrinsic detector efficiencies account for variations in detection efficiency caused by the scintillation medium and the front-end electronics. Several factors can affect the detection efficiency of the scintillators, such as the uniformity of the scintillator material, the volume of the scintillator, the presence of impurities or the room temperature and humidity [20]. Consequently, the intrinsic detector efficiencies can vary through time and in different areas of the scanner. Those factors are computed from the 3-dimensional fan-sum of each detector. Each fan-sum is denoted $\mathcal{S}_{ui}^\epsilon$ and is

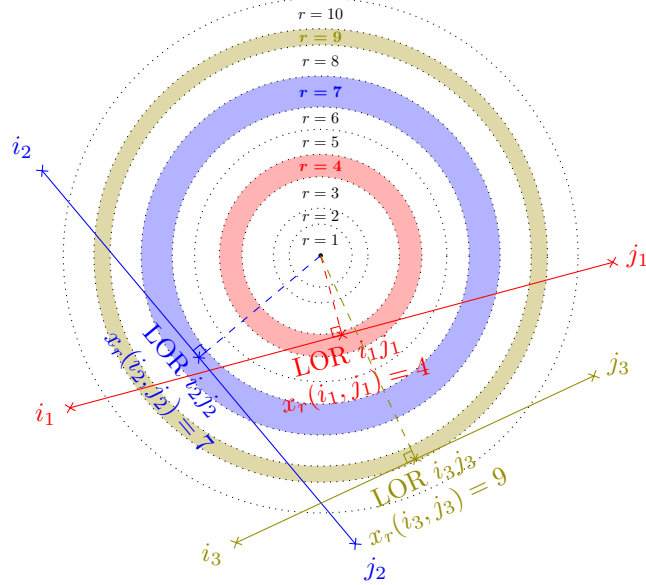


Fig. 4: Example of radial bin decomposition with $K = 10$ bins. Each bin contains the same amount of possible projections LORs. The function $x_r(i, j)$ maps each LOR to its corresponding bin. Here, the radial bin assigned to each sample LOR is highlighted. The axial component (u and v , see Fig. 2) of the LOR is ignored as irrelevant.

defined as

$$\mathcal{S}_{ui}^\epsilon = \sum_{v=1}^M \sum_{j=1}^L t_{uivj}. \quad (16)$$

Finally, using the definition of Eq. (16), the intrinsic detector efficiency ϵ for the detector indexed by axial position u and detector strip i is given by

$$\epsilon_{ui} = \frac{\frac{1}{L} \sum_{i'=1}^L \mathcal{S}_{ui'}^\epsilon}{\mathcal{S}_{ui}^\epsilon}. \quad (17)$$

2.4 Numerical experiments

2.4.1 Monte Carlo simulation parameters

The MC simulations were performed using the Geant4 Application for Tomographic Emission (GATE) [39]. More specifically, we used a modified version of GATE version 9.0, based on Geant4 version 10.6. The tracking of optical photons was not included to limit the computation time. In all the simulations, the β^+ sources decay was simulated as the emission of the back-to-back photon pairs. The direction of the emission was randomized isotropically. The energy of the initial photons was set to 511 keV.

Table 1: Values given to the parameters required to compute the geometrical factors.

| Parameter | Symbol | Value |
|-----------------------|--------|----------------------|
| Number of ring | M | 25 |
| Number of strips | L | $13 \times 24 = 312$ |
| Number of radial bins | K | 25 |

2.4.2 Photon detection, coincidence formation and energy threshold

The front-end electronic response was modelled by the GATE digitizer which converts photon interaction in the scintillator into deposited energy and detection time. In plastic scintillators, unlike inorganic scintillators, photons deposit their energy mainly via Compton scattering. Although not strictly necessary for this study on normalization, energy deposition was simulated with a resolution of 0.231 21 FWHM for an energy of reference of 200 keV, with an energy threshold set to 200 keV (only coincidences with registered energy above the threshold are considered). Coincidences were formed using a coincidence time window of 3 ns was used.

Values of these parameters are realistic with respect to the scanner properties (such as its energy resolution). These values are commonly used for data generation and data analysis in the framework of the J-PET Modular scanner [24, 40].

2.4.3 Scanner geometry

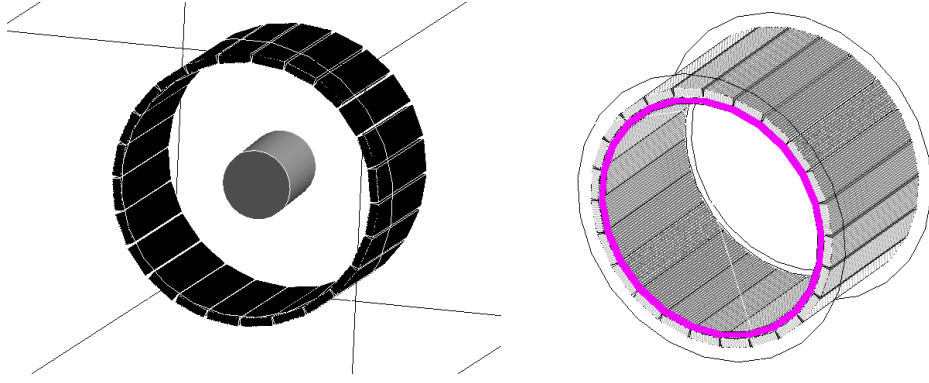
We modelled the geometry of a LAFOV scanner corresponding to the Modular J-PET scanner. The Modular J-PET consists of 24 modules arranged cylindrically with a pitch of 7.5° . Modules form together a cylinder of radius of about 76.2 cm and long of 50 cm. Each module consists of 13 plastic scintillator strips of dimension $24 \text{ mm} \times 6 \text{ mm} \times 500 \text{ mm}$. For MC purposes, the strips were separated into 200 virtual crystals of 2.5 mm in the axial dimension. The geometry of the scanner is shown in Fig. 1b.

The values of the various parameters described in Section 2.2 are summarized in Table 1. The value chosen for L corresponds to the number of strips of the Modular J-PET. The value chosen for M corresponds to axial bins of 25 mm, which is roughly equivalent to the axial resolution of the scanner. Finally, the value chosen for K was chosen empirically, in order to have a satisfactory trade-off between computation speed and result quality.

2.4.4 Phantoms

Three GATE simulations were performed for the analysis presented in this work: 1. a cylindrical phantom and 2. an annular phantom to compute normalization factors; 3. a reference uniform cylinder to compare the uniformity of the reconstructed images.

The cylindrical simulation for normalization was performed during 1800 s using a cylinder long of 50 cm and with a radius of 10 cm, with an activity of 100 MBq. To simplify the analysis and focus on the effects of normalization, the cylinder is composed of a pure source and is therefore free of scattering and attenuation. This simulation is used to compute the block profile factors (b^{ax}), the axial geometric factors (g^{ax}) and



(a) Set-up for the uniform cylinder acquisition. (b) Set-up for the uniform annulus acquisition. The source is located at the pink location (not to scale), and slides in the axial direction.

Fig. 5: Set-ups for the normalization scans.

the intrinsic detector efficiencies (ϵ), as per Eq. (8). The simulation is illustrated in Fig. 5a.

The annular simulation for normalization was performed using a moving annular source. The ring source was 1 cm thick and 2.5 mm long with 10 MBq of activity. A number of 200 positions were simulated along the z axis, each during 100 s, resulting in a total simulation of 20 000 s. Additionally, the radioactive decay of the source was not simulated, to obtain a uniform illumination of the whole scanner. This simulation is used to compute the transverse geometric factors (g^{tr}), as per Eq. (8), because it illuminates the whole FOV, and not only the centre as is the case with the cylindrical simulation. The simulation is illustrated in Fig. 5b.

Finally, a cylindrical phantom filled uniformly with the activity radiotracer was simulated. The phantom was placed symmetrically at the centre of the detector. The length of the cylinder was equal to 400 mm and its radius was set to 100 mm. The shape of a cylinder was chosen for its radial symmetry, which allows the highlighting of potential artefacts resulting from the lack of normalization. The phantom was filled with air to minimize the perturbation incurred by scattered events.

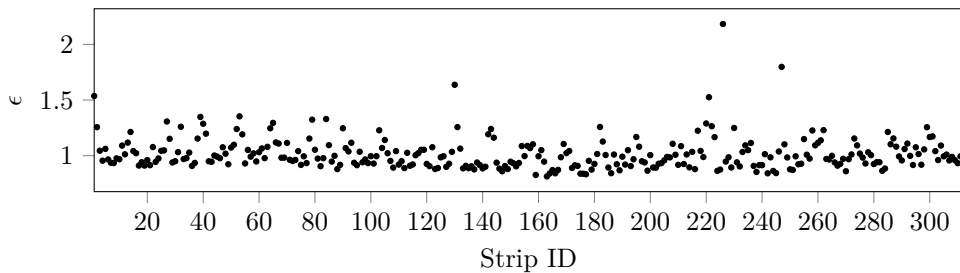
Table 2 summarizes the three MC simulations described above.

2.4.5 Simulation of detection efficiency variations

To study the effects of intrinsic registration efficiency variation per detection unit (factor ϵ , see Eq. (8)), outputs of the GATE simulations were further copied and filtered off-line by a dedicated script applying a MC sampling with the provided relative registration probabilities p_{ui} for all detection units. A coincidence formed of two hits registered in the detector units indexed by (ui, vj) is kept if $r_1 < p_{ui}$ and $r_2 < p_{vj}$, where (r_1, r_2) are random numbers sampled from the uniform distribution $U(0, 1)$. The resulting datasets enable us to study reconstructions of data from a scanner with non-uniform detection efficiency.

Table 2: Summary of all the GATE MC simulations used throughout this work.

| | Normalization cylinder | Normalization annulus | Uniform cylinder |
|---|---------------------------|--------------------------|----------------------|
| Phantom shape | Cylinder | Moving ring | Cylinder |
| Activity | 100 MBq | 10 MBq | 10 MBq |
| Simulation duration | 100 s | 20 000 s | 100 000 s |
| Total number of events, among which: | 31 867 756 | 1 717 907 542 | 2 301 171 650 |
| — true events | 16 223 836 (51 %) | 1 529 567 112 (89 %) | 2 119 859 059 (92 %) |
| — scatter events | 0 (0 %) | 11 251 137 (1 %) | 2 048 690 (< 1 %) |
| — random events | 15 640 357 (49 %) | 176 801 972 (10 %) | 178 810 206 (8 %) |
| — unknown events | 3563 (< 1 %) | 287 321 (< 1 %) | 453 695 (< 1 %) |

**Fig. 6:** Distribution of the detector efficiency factors extracted from the test measurement of the cylindrical phantom performed with the J-PET Modular scanner.

We considered two cases of the relative registration probability variation. The first one consists of an extreme example in which the relative efficiency of a single J-PET module (i.e. 13 consecutive strips, see Fig. 1) was set to 10%. In the second case, the set of detector efficiency probabilities was extracted from a test acquisition of a uniform cylinder phantom by the J-PET Modular scanner. The uniform cylinder was filled with 45 MBq of germanium-68 and positioned at the centre of the detector. The cylinder was tilted by about 3° in the axial direction, but we consider that this small mispositioning is negligible for the current study. The distribution of the efficiency factors is shown in Fig. 6. These efficiencies were further used to filter out our GATE outputs as described above.

2.4.6 Image reconstruction and sensitivity maps computation

Image reconstruction is performed using the Customizable and Advanced Software for Tomographic Reconstruction (CASToR) [41], an emission and transmission tomographic reconstruction software that provides a generic interface to iterative reconstruction algorithms. More specifically, the algorithm used in this work is MLEM operating in list mode, configured to stop at 30 iterations. The image size is set to be $320 \times 320 \times 200$ voxels of 2.5 mm^3 each. The resulting image spans 800 mm^2 in

the transverse direction, and 500 mm in the axial direction, which completely encompasses the FOV of the Modular J-PET detector (see Section 1). The projector used is a raytracing projector that uses the incremental Siddon algorithm [42] along each line. The raytracing projector was set to use 10 rays. The reconstruction procedure does not take into account any additional resolution modelling.

The sensitivity map is generated before the reconstruction. Two sensitivity maps were considered:

1. An analytical sensitivity map that does not incorporate any normalization factors. This sensitivity map is purely geometric and models the solid angle of the centre of each voxel. More details are given in Section A.
2. A sensitivity map reflecting the geometrical properties based on detector positions (which only models $\mathbf{A}^{\text{scanner}}$ of Eq. (2)), to which several sets of normalization factors are incorporated. This sensitivity map is computed directly using CASToR.

2.4.7 Metrics for image quality assessment

The factor U_{axial} is used to assess the axial uniformity of the reconstruction. The image of the reference cylinder is divided axially into 11 slices. Each slice has a thickness of 13 voxels. Next, the mean intensity value of each slice is computed. The determined values are gathered in a set of means S_{axial} . The axial uniformity is then given by

$$U_{\text{axial}} = \frac{\max(S_{\text{axial}}) - \min(S_{\text{axial}})}{\text{mean}(S_{\text{axial}})} \quad (18)$$

Analogically, the factor U_{radial} is used to assess the radial uniformity of the reconstruction. The image of the reference cylinder is divided into 15 radial bins such that each bin contains approximately the same number of voxels (see Fig. 4). As in Eq. (18), the mean intensity value of each bin is computed. The determined values are gathered in a set of means S_{radial} . The radial uniformity is defined as

$$U_{\text{radial}} = \frac{\max(S_{\text{radial}}) - \min(S_{\text{radial}})}{\text{mean}(S_{\text{radial}})} \quad (19)$$

By construction the U_{axial} and U_{radial} are non-negative real numbers. The ideal uniformity corresponds to the situation when U_{axial} (U_{radial}) values are equal to 0. To further analyse the variation of the uniformity we define a ratio per axial slice:

$$R(u) = \frac{\text{std}(u)}{\text{mean}(u)} \quad (20)$$

where u index denotes a slice in the axial direction and std and mean are the corresponding standard deviation and mean calculated for a given slice u . Again, $R = 0$ corresponds to the ideal, uniform image.

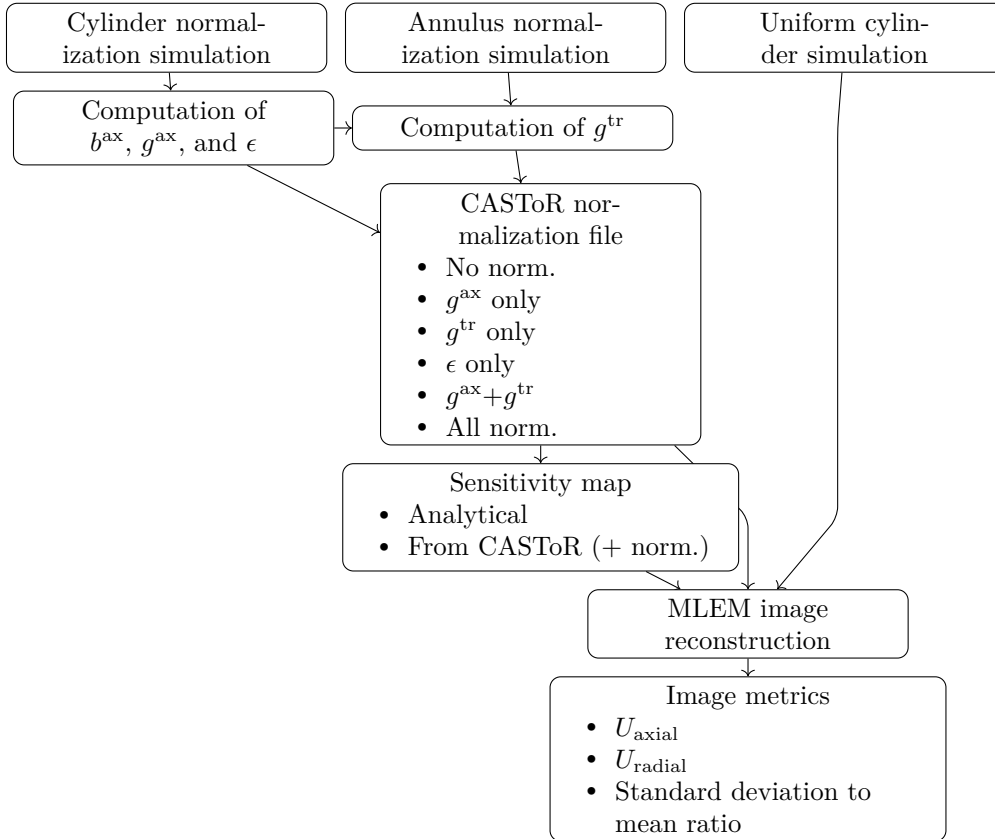


Fig. 7: Workflow of the analysis conducted in this work.

2.4.8 Scheme of the analysis flow

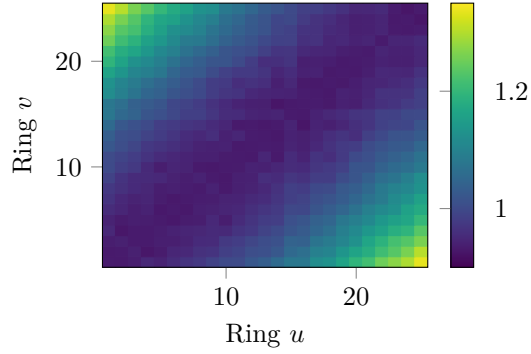
Figure 7 summarizes the normalization factor computation and analysis flow detailed in Sections 2.4.1 and 2.4.5 to 2.4.7.

3 Results

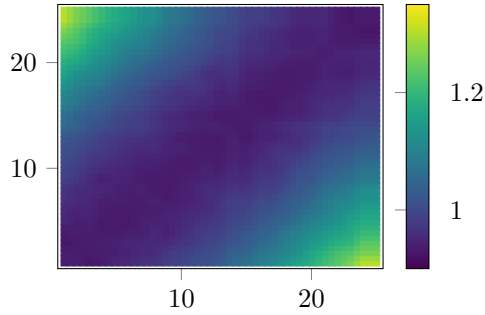
3.1 Normalization factor distributions

Figure 8a presents the axial geometric factors computed based on the MC simulations of the cylindrical acquisition described in Section 2.4.1. The reduced efficiency for LORs with large ring difference $|u - v|$ results in higher axial geometric factors at the edges. Figure 8b shows the bilinear interpolation of these axial geometric factors, which is used to compute them for LORs with arbitrary obliqueness in the axial direction.

Figure 9 illustrates the transverse geometric factors estimated based on the MC simulations of the annular acquisition (Section 2.4.1). We observe higher normalization values near the centre of the detector. A third-degree polynomial is also displayed.



(a) Axial geometric factors (g^{ax}).



(b) Bilinear interpolation of the axial geometric factors.

Fig. 8: Axial geometric factors and its interpolation.

This fit is used to calculate the radial geometric factor for LORs of an arbitrary radial position.

Figure 10a depicts the intrinsic detector efficiencies derived from the MC simulations of the cylindrical acquisition (Section 2.4.1). Since the simulation model assumes perfect detectors with uniform efficiencies, the resulting factors are distributed uniformly around unity, with the small variations attributed solely to statistical noise.

Figure 10b shows the intrinsic detector efficiencies distribution, where one detector has 10% lower efficiency (see Section 2.4.5). The region affected by the reduced efficiency is visible and the values of the normalization factors match the intensity of the lowered efficiency. Interestingly, we notice that the small region located around $i \approx 163$ exhibits higher normalization factors because these detectors are frequently in coincidence with the first module, with the reduced efficiency.

3.2 Reconstructed images of the reference cylinder

The comparison of the reconstructed images of the uniform cylindrical phantom (see Section 2.4.1) is shown in Fig. 11. Without normalization, artefacts appear at the

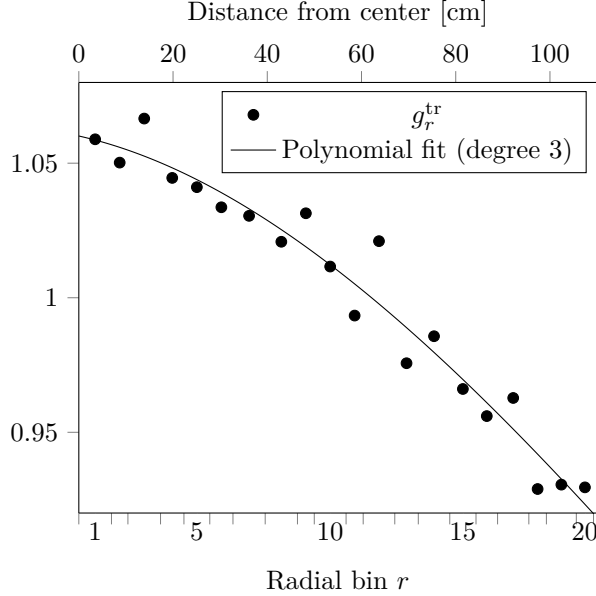


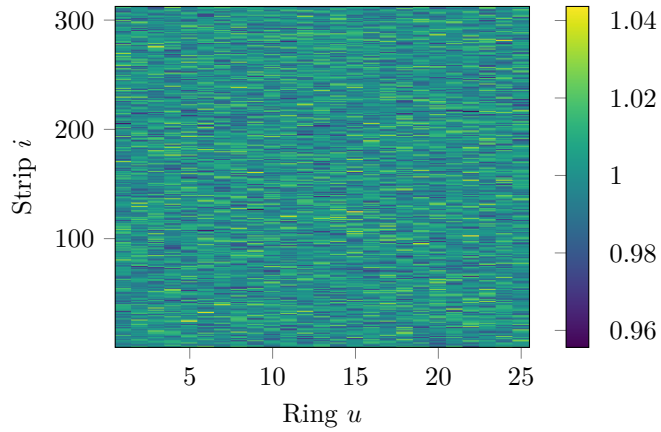
Fig. 9: Transverse geometric factors g_r^{tr} with a polynomial fit of degree 3. Coefficients of the polynomial fit are 2.253×10^{-8} , -1.060×10^{-5} , -3.958×10^{-4} and 1.060.

centre of the cylinder as a dip. Applying axial and radial corrections considerably reduces those effects.

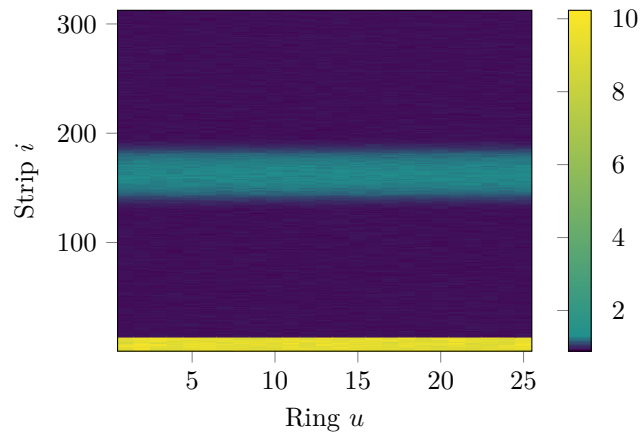
3.3 Studies of geometric effects

To get further insight we plotted the uniformity metrics U_{axial} and U_{radial} as a function of iteration number for reconstructions performed with different sensitivity maps, as presented in Fig. 12. For all variants, U_{axial} reaches the plateau around the 10th iteration. A similar trend is observed for U_{radial} , except for the reconstruction with an analytical sensitivity map, where the non-uniformity continues to rise with the number of iterations. On the plot, it is clearly seen that even the usage of an analytical sensitivity map yields a huge improvement in reconstruction uniformity from 0.85 to 0.15 in terms of U_{axial} . Additionally, the geometrical normalization factors improve the reconstruction quality even further. As expected axial normalization factors work better in the axial direction reaching the uniformity level U_{axial} below 0.02, whereas radial normalization factors improve the uniformity in the radial direction U_{radial} below 0.15. It is interesting to note, that the application of both corrections at the same time gives a slightly more non-uniform image in the radial direction $U_{\text{radial}} \approx 0.18$. On the other hand, visual inspection of the reconstructed image suggests that the two normalization factors, when applied together, give the most uniform reconstruction, as highlighted in Fig. 11.

Figure 13 shows the standard deviation to mean ratio for each slice of the reconstructed cylinder (see Fig. 11). Lower values correspond to more uniform slices. The



(a) Intrinsic detector efficiencies with uniform detector efficiency. The variations are due to statistical noise.



(b) Intrinsic detector efficiencies when the first module (the first 13 strips) have an efficiency of 10%. The resulting normalization factors are thus 10 times higher in this region of the detectors, and somewhat higher also for scintillators located in front of the deficient module. The color scale is non-linear in order to highlight this effect.

Fig. 10: Intrinsic detector efficiencies (ϵ).

figure illustrates that normalization factors favourably compensate for the image artefacts and improve the uniformity of the resulting reconstructed images. However, it does not fully remove the dependence of the uniformity on the slice position. Namely, the slices located on the edges of the detector are more non-uniform compared to the centre ones. The shape of the curves, along with the obtained range of values (5.5% to 8.5% in the case of the reconstruction performed with all normalization factors), are in agreement with similar studies conducted by other groups [43].

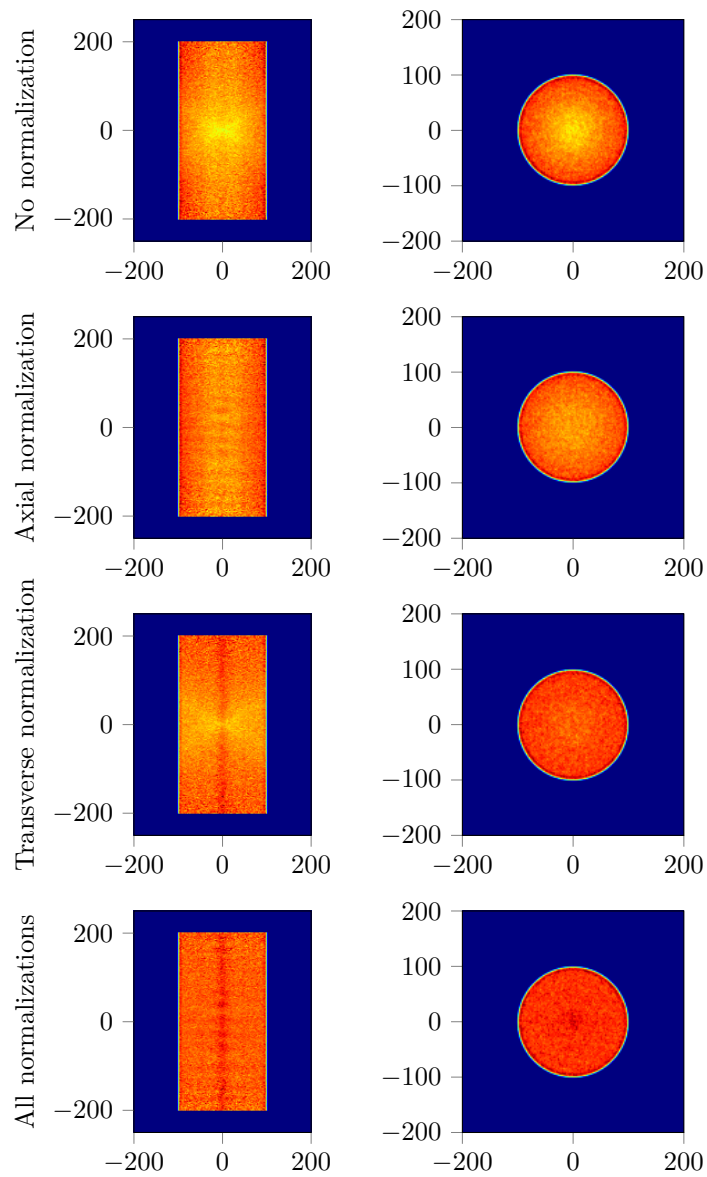


Fig. 11: MLEM reconstruction (30th iteration) of the uniform cylinder with four different sets of normalization factors applied. Left column: central xz (axial) plane. Right column: central xy (transverse) plane.

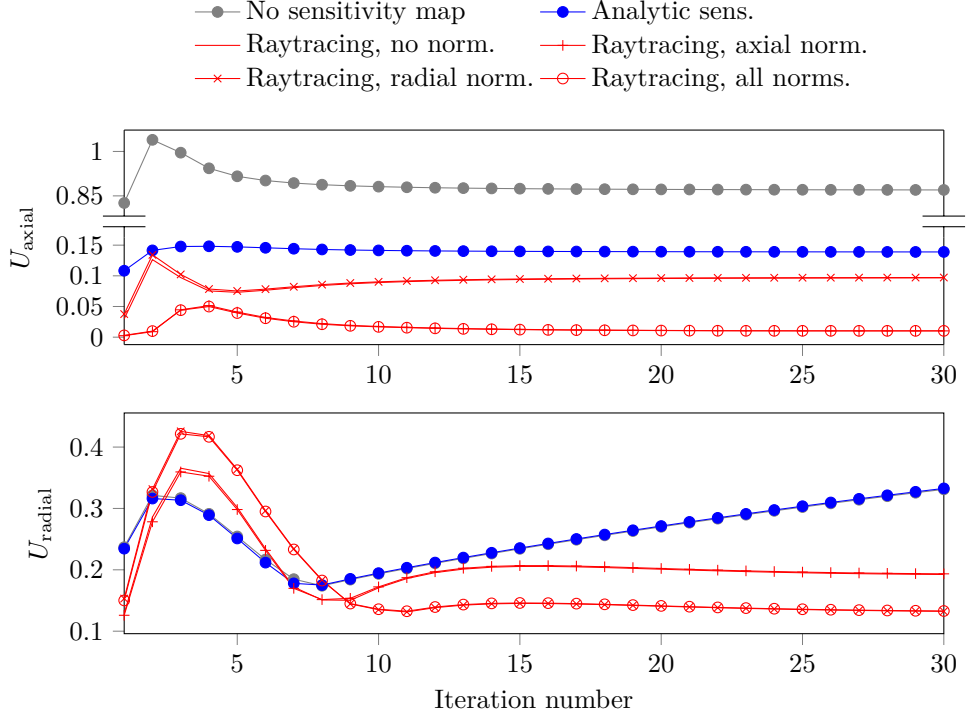


Fig. 12: U_{axial} and U_{radial} with respect to iteration number. Lower values mean more uniform reconstructions in the given direction.

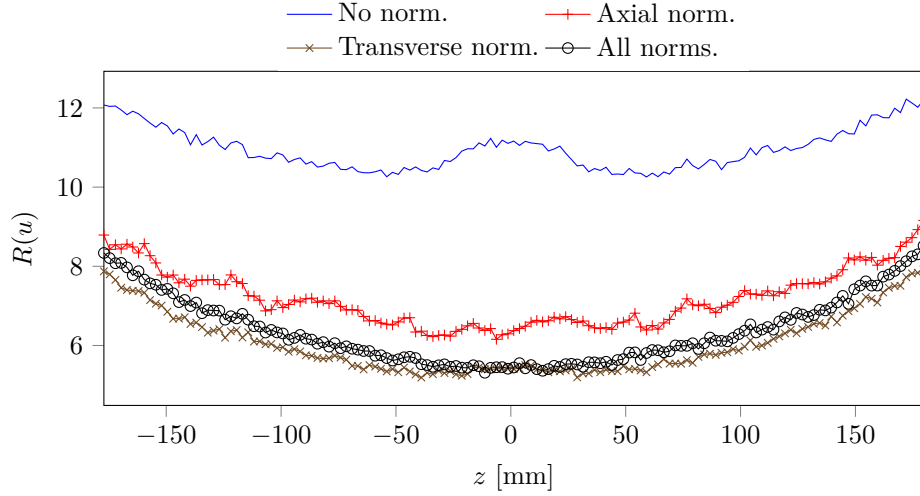


Fig. 13: Standard deviation to mean ratio (Eq. (20)) calculated per slice as a function of the axial position z .

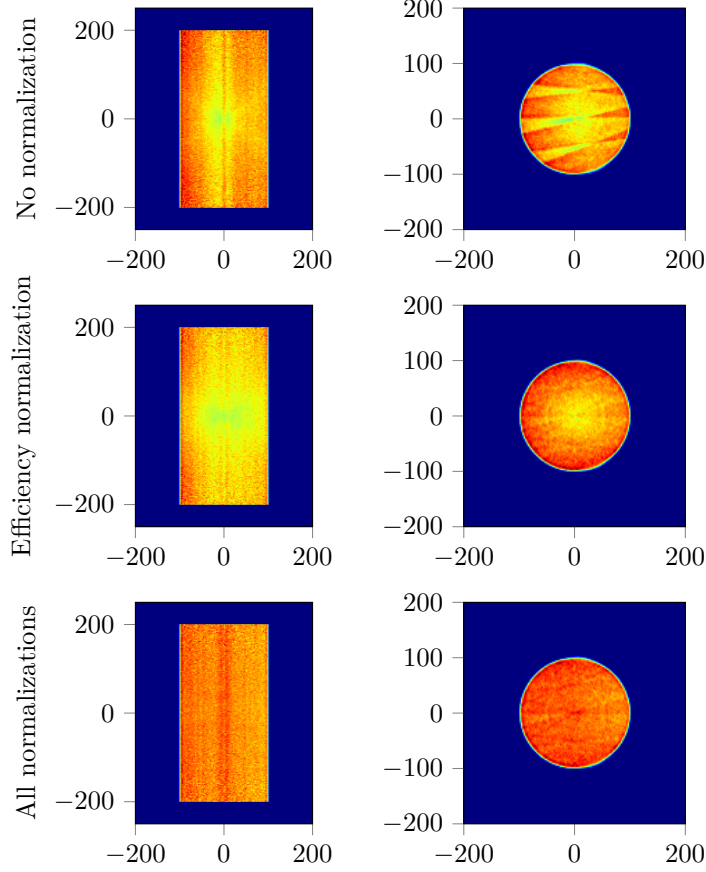


Fig. 14: MLEM reconstruction (30th iteration) of the uniform cylinder with the first detector module set at 10% efficiency. Left column: central xz (axial) plane. Right column: central xy (transverse) plane.

3.4 Studies of intrinsic efficiency variation effects

Figure 14 shows reconstructions performed from the data that simulate a lowered efficiency of the first module (see Section 2.4.5). Although strong artefacts appear when the reconstruction is done without normalization factors, the efficiency factors (shown in Fig. 10b) favourably compensate for these artefacts and produce an improved final reconstruction. Interestingly, when applying the efficiency normalization only, without geometric normalization, the resulting image displays a dip in the centre, just as in Fig. 11.

Figure 15 shows reconstructions performed with realistic detector efficiencies estimated from an actual measurement. Again we notice that incorporating efficiency normalization coefficients compensates for the artefacts present in the non-normalization image, but the typical dip due to the lack of (axial and transverse) geometrical

Table 3: Summary of computation times for the two normalization MC simulations.

| | Cylindrical simulation | Annular simulation |
|--|---|--|
| Computed normalization factors | b^{ax} (Eq. (9)), g^{ax} (Eq. (11)) and ϵ (Eq. (16)) | g^{tr} (Eq. (13)) |
| Number of output files | 1000 | 1000 |
| Number of coincidences per output file | About 3.2×10^4 | 1.3×10^5 to 2.2×10^6 |
| Total number of coincidences | 31 867 756 | 1 717 907 542 |
| Processing time per file (on a 2.8 GHz core) | 37 s | 31 min |
| Total CPU time | 10 h | 516 h |
| Total clock time | 111 s | 93 min |

normalization is still visible. Finally, when using both geometrical and efficiency normalization, those effects are mitigated.

3.5 Processing times

All the computations were performed using the Świerk Computing Centre (CIŚ) cluster, the computing centre of the National Center for Nuclear Research located in Poland. We designed our scripts that compute normalization factors to benefit from CIŚ parallel infrastructure, allowing us to process the files in parallel and reduce the total processing time, as detailed in Table 3. The large difference in processing time between the cylindrical and the annular simulations is explained by the fact that the annular simulation produces many more coincidences due to the source lying extremely close to the detectors.

The reconstructions were performed at CIŚ on 40 2.8 GHz cores using CASToR compiled with threading support. Using the raytracing projector, reconstructions took a long period of time due to the 10 rays that were calculated per projection: each iteration took approximately 17 700 s, and the whole reconstruction (30 iterations) lasted 152 h.

3.6 Towards total-body J-PET

The main difficulty for computing the normalization factors for TB J-PET is the amount of LORs. Assuming axial virtual crystals of 20 mm, the Modular J-PET consists of 30 416 100 possible LORs (without assuming any restricted FOV), whereas the TB J-PET, with its total of 7 rings, consists of 1 490 552 700 possible LORs, which corresponds to a 7^2 -fold increase in the number of LORs.

Our current implementation stores the normalization factors in a CASToR normalization data file, which requires one floating-point number (32 bits) for the normalization factor plus two integers (64 bits) for the detector IDs. Therefore, each normalization factor requires 96 bits, which results in data files of approximately 365 MB for the Modular J-PET, and data files of 17.9 GB for the TB J-PET. Although

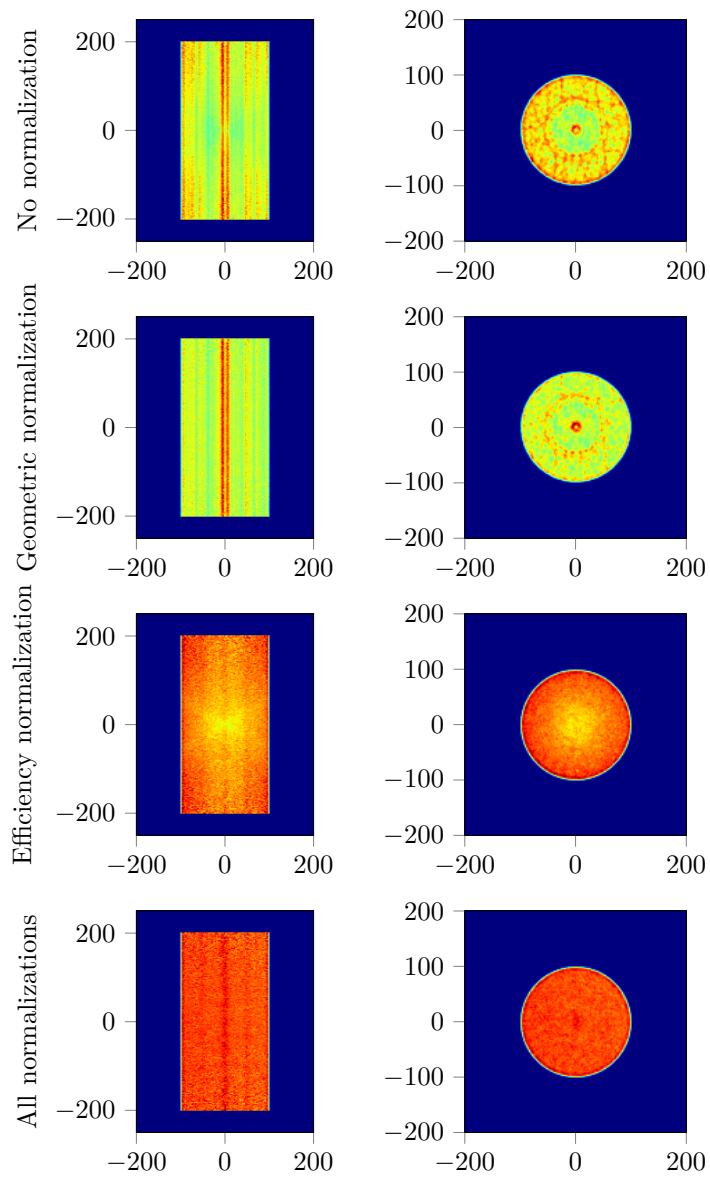


Fig. 15: MLEM reconstruction (30th iteration) of the uniform cylinder with realistic efficiencies. Left column: central xz (axial) plane. Right column: central xy (transverse) plane.

much larger, such a file size is still manageable, and in the worst-case scenario CAS-ToR could be modified to handle smaller files, for instance by providing a default value for LORs outside some FOV instead of storing them in the normalization file.

Regarding computation times, for the Modular J-PET, processing the cylindrical simulation took 111 s, and the annular simulation 93 min (Section 3.5). Extrapolating this number to the TB J-PET, taking into account that it possesses 49 times more LORs, would yield computation times of 5439 s (1.5108 h) for the cylindrical simulation, and 4557 min (75.95 h) for the annular simulation. Although longer, such computation times are still tenable because geometrical normalization factors need to be computed only once as they do not evolve through time.

Additionally, and even though computations could realistically be carried out, reducing the statistics of the normalization measurements for the TB J-PET seems acceptable. For instance, according to Table B1, reducing the statistics of normalization measurements by 90 % would correspond to an error of about 2.51 % only, while roughly speeding-up computations times by a factor of 10. This is due to the fact that component-based normalization is a method known for largely reducing the variance of the computed normalization factors, which makes it particularly suited for TB J-PET normalization with lowered statistics. Also, in this case, it is beneficial to remove the most oblique LORs which are anyway mostly affected by multiple scattering and depth-of-interaction uncertainty [3].

4 Summary and Outlook

We implemented a normalization correction procedure adapted for the plastic-based J-PET Modular scanner, using the CBN method. In our studies, we considered both the geometric and detection efficiency factors. We estimated the geometric normalization factors for the J-PET Modular scanner using MC simulations. We also analysed the effects of variations in detection efficiency. A dedicated cylindrical phantom was simulated to investigate the impact of various factors on image quality. The image uniformity was quantified in terms of U_{axial} , U_{radial} and R metrics, calculated for a set of image slices. The results demonstrate that the component-based normalization method is well-suited for the Modular J-PET scanner.

Without normalization, reconstructions of a uniform cylinder exhibit artefacts in the form of a dip located at the centre of the cylinder. The application of axial and radial geometric corrections favourably compensates for the image artefacts and improves the image uniformity. However, a slight dependence on the image slice axial position remains. This variability expressed as a standard deviation-to-mean ratio (see Figure 13) ranging between 5.5 % to 8.5 %, and agrees with similar studies conducted by other groups [43]. In the case of variable detector efficiencies, several more pronounced artefacts appear. These artefacts were also satisfactorily compensated using the efficiency normalization factors.

To validate the robustness of the method, we performed several systematic checks, detailed in Section B. We also examined the impact of the gathered statistics on the stability of the normalization factor distributions. Additionally, we conducted a test

using a cylinder phantom to compute transverse geometrical factor (g^{tr}), to cross-check if the procedure could be further simplified by requiring a single acquisition.

Computationally, the technique is straightforward to parallelize, making it time-efficient. The component-based normalization approach is also expected to be suitable for the next-generation 2 m-long scanner currently being developed at the Jagiellonian University. The normalization factors are likely to be even more beneficial for images reconstructed from data acquired by this scanner due to the extended axial dimension, which amplifies the geometrical effects. Preliminary estimates of computing times and memory requirements suggest that the method is appropriate for use with this larger scanner.

In future work, we plan to develop a protocol for acquiring normalization scans together with the dedicated phantoms. Further work will involve extension of the normalization correction procedure as well as code optimization given the processing time for the prototype of the TB J-PET scanner currently under construction. Moreover, the normalization model will be extended for positronium imaging which requires registration and analysis of coincidences formed from two annihilation photons and one high-energetic gamma [32, 33].

5 Author Contribution

The concept of the article was conceived by W.K. The figures were conceptualized by A.C. and W.K. The analytical model of sensitivity was prepared by W.K. The MC simulations were performed by Sz.P. and J.B. The data selection, normalization estimates and image reconstruction were conducted by A.C. under the supervision of W.K. The analysis of the results and quality metrics was performed by A.C. and W.K. K. Klimaszewski, W.W., L.R., and R.Y.S. managed the computing resources for simulations. The main financial support was provided by P.M. The manuscript was prepared by A.C. and W.K. and was then edited and approved by all authors.

6 Acknowledgements

The authors would like to acknowledge the technical support from A. Heczko, M. Kajetanowicz, and W. Migdał. A.C. would like to thank Dr. A. Gajos for providing the experimental data sample used for efficiency variation studies. This work was completed with resources provided by the Świerk Computing Centre at the National Centre for Nuclear Research. We acknowledge the support provided by the National Science Centre of Poland through grants no. 2021/42/A/ST2/00423 (P.M.), 2021/43/B/ST2/02150 (P.M.), 2022/47/I/NZ7/03112 (E.Ł.S) and 2021/41/N/ST2/03950 (K.D.); the Ministry of Education and Science through grants no. SPUB/SP/490528/2021 (P.M.), IAL/SP/596235/2023 (P.M.); as well as the SciMat and qLife Priority Research Area budgets under the programme Excellence Initiative - Research University at the Jagiellonian University (P.M.).

Appendix A Analytical model of sensitivity

We introduce a simple analytical model of the sensitivity distribution S in the image space for the idealized cylindrical scanner defined by the radius R and the axial length L . It serves as a reference for further more complex models. The model is constructed with several simplifications, the main one consists of the assumption that the sensitivity can be factorized into the geometry-dependent term, and a space-invariant term K incorporating all other effects including the detection efficiency of the coincidence pair and the energy selection efficiency:

$$S(x, y, z) = K \cdot A(x, y, z). \quad (\text{A1})$$

Due to the system symmetry, it is useful to use the cylindrical coordinates (ρ, z) . By construction, the following dependency is fulfilled:

$$A(\rho, z) = A(\rho, -z). \quad (\text{A2})$$

We determine the geometrical acceptance part by calculating the fraction of the solid angles “seen” from the given spatial point (ρ, z) within the scanner. The model $A(\rho, z)$ is given by:

$$A(\rho, z) = \begin{cases} \frac{\frac{L}{2}-z}{2} \left(\frac{1}{\sqrt{(\frac{L}{2}-z)^2+(R-\rho)^2}} + \frac{1}{\sqrt{(\frac{L}{2}-z)^2+(R+\rho)^2}} \right) & \text{if } z > \rho \frac{L}{2R} \\ \frac{\frac{L}{2}+z}{2} \left(\frac{1}{\sqrt{(\frac{L}{2}+z)^2+(R+\rho)^2}} + \frac{1}{\sqrt{(\frac{L}{2}+z)^2+(R-\rho)^2}} \right) & \text{if } z < -\rho \frac{L}{2R} \\ 0 & \text{otherwise} \end{cases}. \quad (\text{A3})$$

For $(\rho = 0, z = 0)$, the equation reduces to the known formula of the system sensitivity for the point source placed in the centre of the scanner [44]:

$$S(0, 0) = K \cdot \frac{L}{2} \left(\frac{1}{\sqrt{(\frac{L}{2})^2 + R^2}} \right) = K \cdot \sin \left(\arctan \left(\frac{L}{2R} \right) \right). \quad (\text{A4})$$

Appendix B Additional verifications

In addition to the results presented in Section 3, we have performed several systematic verifications to ensure that the method is sufficiently robust and that the results shown are not only valid for the specific set of parameters that were used. More specifically, we have:

- Changed the widths of axial (M) and radial (K) bins (see Section 2.2). Although finer binning would theoretically correspond to a normalization of greater quality, in practice we did not notice any important improvements. The current parameter values, as given in Table 1, seem to be well-suited for our application to the Modular J-PET scanner.

- Checked whether a single bin would be enough in the axial direction (i.e. set $M = 1$), which would better describe the geometry of the Modular J-PET scanner built up from long scintillator strips. Although preliminary results seemed interesting, we decided to focus here on results with virtual crystals in the axial direction ($M > 1$) in order to better match Ref. [38]. Moreover, a single axial bin would reduce the computational burden which would specifically benefit the normalization of the TB J-PET scanner (see Section 3.6). Assessing the realism of this approach in more detail will be the subject of future work.
- Checked how the method behaves changing the data smearing. More precisely, we have moved the hit positions to the strip centres for the x and y coordinates, and have smeared the z position of the hits with a Gaussian smoothing of standard deviation $\sigma = 10$ mm, which is roughly equivalent to the axial resolution of the Modular J-PET. Although the effects of smearing were apparent on the reconstructed images, the values of the normalization factors did not change by any noticeable amount.
- Tried different reconstruction parameters, and more precisely changed the projector and the number of iterations. Concerning the projectors, Fig. C1 shows some results that compare two different projectors. Concerning the number of iterations, we ensured that the results did not evolve significantly after the 30th iteration, which is why only 30 iterations are shown in Figs. C1 and 12.
- Checked if one simulation (or acquisition) would suffice, instead of the two simulations currently used by our current methodology (cylindrical and annular, see Fig. 5), as justified by Section 2.4.4 and Ref. [38]. Indeed, for a real on-device measurement, it would be more convenient to perform a single acquisition. We checked how the results changed when using the cylindrical acquisition to compute all normalization factors, and although this approach reduces the FOV of the scanner to the size of the cylinder, reconstructed images were still of satisfactory quality. For future works, we plan to only use the annular acquisition to perform reconstructions and compare the reconstructions against those obtained from the cylinder acquisition. We also plan to establish which of these set-ups would be easier to perform on the device.
- Compared the quality of reconstructions obtained from the CASToR-based sensitivity maps with reconstructions obtained from a sensitivity map purely computed from a MC simulation. The MC simulation consisted of a high-statistics acquisition of a uniform cylinder that completely filled the scanner FOV. We noticed that the CASToR-based sensitivity maps seemed to give slightly better results than the pure MC-based sensitivity map.

Table B1 shows the relative differences between the normalization coefficients obtained from high statistic normalization scan and several other smaller normalization scans. This table highlights the robustness of the component-based normalization method: even with as little as 10% of the total statistics, the normalization coefficients vary on average only by about 2.51% compared to their value obtained from full statistics.

Table B1: Relative difference in percentage for the normalization coefficients as a function of the number of true coincidences per normalization scan.

| True coincidences | Difference percentage |
|-------------------|-----------------------|
| 10% | 2.506 ± 1.943 |
| 25% | 1.429 ± 1.098 |
| 50% | 0.8887 ± 0.6947 |
| 100% | (Reference) |

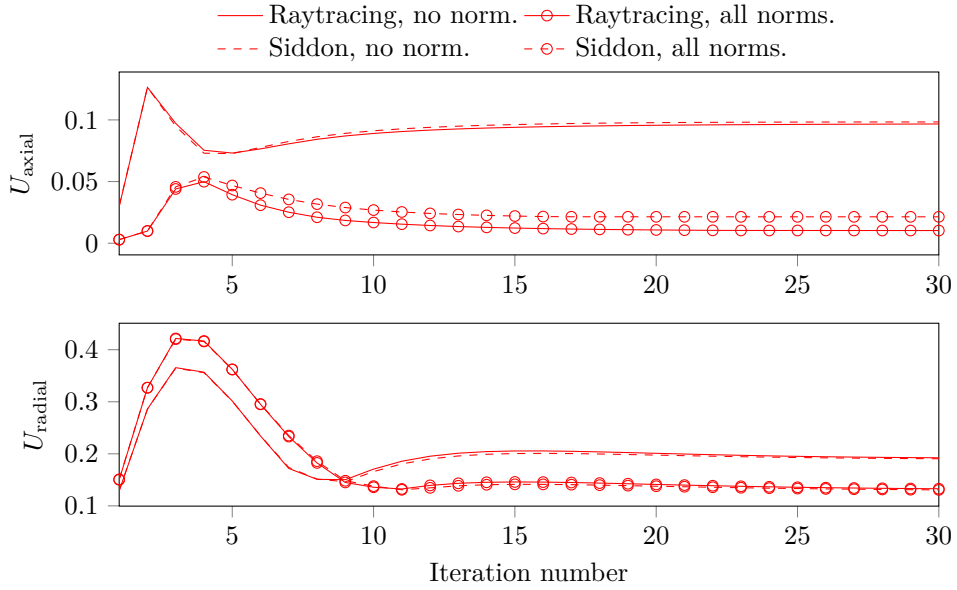


Fig. C1: U_{axial} and U_{radial} with respect to iteration number for raytracing and Siddon projectors. Lower values mean more uniform reconstructions in the given direction.

Appendix C Influence on the projector choice

Two different projectors are used: the Siddon projector [45] and a raytracing projector that uses the incremental Siddon algorithm [42] along each line. The raytracing projector uses 10 rays.

Figure C1 shows the evolution of U_{axial} and U_{radial} with respect to iteration number for reconstructions achieved with the Siddon projector and with the raytracing projector. The figure highlights that using the raytracing projector produces images of higher uniformity, as expected from a projector that shoots more rays compared to the Siddon projector.

References

- [1] Alberts, I., Sari, H., Mingels, C., Afshar-Oromieh, A., Pyka, T., Shi, K., Rominger, A.: Long-axial field-of-view PET/CT: Perspectives and review of a revolutionary development in nuclear medicine based on clinical experience in over 7000 patients. *Cancer Imaging* **23**(1), 28 (2023) <https://doi.org/10.1186/s40644-023-00540-3>
- [2] Badawi, R.D., Shi, H., Hu, P., Chen, S., Xu, T., Price, P.M., Ding, Y., Spencer, B.A., Nardo, L., Liu, W., Bao, J., Jones, T., Li, H., Cherry, S.R.: First human imaging studies with the EXPLORER total-body PET scanner. *J Nucl Med* **60**(3), 299–303 (2019) <https://doi.org/10.2967/jnumed.119.226498>
- [3] Qi, J., Matej, S., Wang, G., Zhang, X.: 3D/4D reconstruction and quantitative total body imaging. *PET Clinics* **16**(1), 41–54 (2021) <https://doi.org/10.1016/j.cpet.2020.09.008>
- [4] Efthimiou, N.: New challenges for PET image reconstruction for total-body imaging. *PET Clinics* **15**(4), 453–461 (2020) <https://doi.org/10.1016/j.cpet.2020.06.002>
- [5] Iriarte, A., Marabini, R., Matej, S., Sorzano, C.O.S., Lewitt, R.M.: System models for PET statistical iterative reconstruction: A review. *Computerized Medical Imaging and Graphics* **48**, 30–48 (2016) <https://doi.org/10.1016/j.compmedimag.2015.12.003>
- [6] Badawi, R.D., Lodge, M.A., Marsden, P.K.: Algorithms for calculating detector efficiency normalization coefficients for true coincidences in 3D PET. *Phys. Med. Biol.* **43**(1), 189–205 (1998) <https://doi.org/10.1088/0031-9155/43/1/012>
- [7] Badawi, R.D., Marsden, P.K.: Developments in component-based normalization for 3D PET. *Phys. Med. Biol.* **44**(2), 571–594 (1999) <https://doi.org/10.1088/0031-9155/44/2/020>
- [8] Defrise, M., Townsend, D.W., Bailey, D., Geissbuhler, A.M.C., Jones, T.: A normalization technique for 3D PET data. *Phys. Med. Biol.* **36**(7), 939–952 (1991) <https://doi.org/10.1088/0031-9155/36/7/003>
- [9] Bai, B., Li, Q., Holdsworth, C.H., Asma, E., Tai, Y.C., Chatziioannou, A., Leahy, R.M.: Model-based normalization for iterative 3D PET image reconstruction. *Phys. Med. Biol.* **47**(15), 2773–2784 (2002) <https://doi.org/10.1088/0031-9155/47/15/316>
- [10] Vicente, E., Vaquero, J.J., Espana, S., Herraiz, J.L., Udias, J.M., Desco, M.: Normalization in 3D PET: Dependence on the activity distribution of the source. In: 2006 IEEE Nuclear Science Symposium Conference Record, pp. 2206–2209. IEEE, San Diego, CA, USA (2006). <https://doi.org/10.1109/NSSMIC.2006.354352>

- [11] Hoffman, E.J., Guerrero, T.M., Germano, G., Digby, W.M., Dahlbom, M.: PET system calibrations and corrections for quantitative and spatially accurate images. *IEEE Trans. Nucl. Sci.* **36**(1), 1108–1112 (1989) <https://doi.org/10.1109/23.34613>
- [12] Watson, C.C.: Co-fan-sum ratio algorithm for randoms smoothing and detector normalization in PET. In: *IEEE Nuclear Science Symposium & Medical Imaging Conference*, pp. 3326–3329. IEEE, Knoxville, TN (2010). <https://doi.org/10.1109/NSSMIC.2010.5874420>
- [13] Bailey, D.L., Townsend, D.W., Kinahan, P.E., Grootenok, S., Jones, T.: An investigation of factors affecting detector and geometric correction in normalization of 3-D PET data. *IEEE Trans. Nucl. Sci.* **43**(6), 3300–3307 (Dec./1996) <https://doi.org/10.1109/23.552739>
- [14] Hogg, D., Thielemans, K., Spinks, T., Spyrou, N.: Maximum-likelihood estimation of normalisation factors for PET. In: *2001 IEEE Nuclear Science Symposium Conference Record (Cat. No.01CH37310)*, vol. 4, pp. 2065–2069. IEEE, San Diego, CA, USA (2002). <https://doi.org/10.1109/NSSMIC.2001.1009231>
- [15] Wang, W., Hu, Z., Gagnon, D.: A new component approach to efficiency normalization for 3D PET. *IEEE Trans. Nucl. Sci.* **54**(1), 92–99 (2007) <https://doi.org/10.1109/TNS.2006.887468>
- [16] Belzunce, M.A., Reader, A.J.: Time-invariant component-based normalization for a simultaneous PET-MR scanner. *Phys. Med. Biol.* **61**(9), 3554–3571 (2016) <https://doi.org/10.1088/0031-9155/61/9/3554>
- [17] Belzunce, M.A., Reader, A.J.: Self-normalization of 3D PET data by estimating scan-dependent effective crystal efficiencies. In: *2015 IEEE Nuclear Science Symposium and Medical Imaging Conference (NSS/MIC)*, pp. 1–3. IEEE, San Diego, CA, USA (2015). <https://doi.org/10.1109/NSSMIC.2015.7582049>
- [18] W Zhou, V., Kyme, A.Z., Meikle, S.R., Fulton, R.: A scheme for PET data normalization in event-based motion correction. *Phys. Med. Biol.* **54**(17), 5321–5339 (2009) <https://doi.org/10.1088/0031-9155/54/17/016>
- [19] Panin, V.Y., Smith, A.M., Casey, M.E.: Normalization coefficient computing for continuous bed motion acquisition. In: *2013 IEEE Nuclear Science Symposium and Medical Imaging Conference (2013 NSS/MIC)*, pp. 1–10. IEEE, Seoul, Korea (South) (2013). <https://doi.org/10.1109/NSSMIC.2013.6829402>
- [20] Theodorakis, L., Loudos, G., Prassopoulos, V., Kappas, C., Tsougos, I., Georgoulas, P.: A review of PET normalization: Striving for count rate uniformity. *Nuclear Medicine Communications* **34**(11), 1033–1045 (2013) <https://doi.org/10.1097/MNM.0b013e328365ac1e>

- [21] Prenosil, G.A., Sari, H., Fürstner, M., Afshar-Oromieh, A., Shi, K., Rominger, A., Hentschel, M.: Performance characteristics of the Biograph Vision Quadra PET/CT system with a long axial field of view using the NEMA NU 2-2018 standard. *J Nucl Med* **63**(3), 476–484 (2022) <https://doi.org/10.2967/jnumed.121.261972>
- [22] Karp, J.S., Viswanath, V., Geagan, M.J., Muehllehner, G., Pantel, A.R., Parma, M.J., Perkins, A.E., Schmall, J.P., Werner, M.E., Daube-Witherspoon, M.E.: PennPET Explorer: Design and preliminary performance of a whole-body imager. *J Nucl Med* **61**(1), 136–143 (2020) <https://doi.org/10.2967/jnumed.119.229997>
- [23] Tayefi Ardebili, F., Niedźwiecki, S., Moskal, P.: Evaluation of modular J-PET sensitivity. *Bio-Algorithms and Med-Systems* **19**(1), 132–138 (2023) <https://doi.org/10.5604/01.3001.0054.1973>
- [24] Moskal, P., Kowalski, P., Shopa, R.Y., Raczyński, L., Baran, J., Chug, N., Curceanu, C., Czerwiński, E., Dadgar, M., Dulski, K., Gajos, A., Hiesmayr, B.C., Kacprzak, K., Kapłon, Ł., Kisielewska, D., Klimaszewski, K., Kopka, P., Korcyl, G., Krawczyk, N., Krzemień, W., Kubicz, E., Niedźwiecki, S., Parzych, S., Raj, J., Sharma, S., Shivani, S., Stępień, E., Tayefi, F., Wiślicki, W.: Simulating NEMA characteristics of the modular total-body J-PET scanner—an economic total-body PET from plastic scintillators. *Phys. Med. Biol.* **66**(17), 175015 (2021) <https://doi.org/10.1088/1361-6560/ac16bd>
- [25] Moskal, P., Alfs, D., Bednarski, T., Białas, P., Czerwiński, E., Curceanu, C., Gajos, A., Głowacz, B., Gorgol, M., Hiesmayr, B.C., Jasińska, B., Kamińska, D., Korcyl, G., Kowalski, P., Kozik, T., Krzemień, W., Krawczyk, N., Kubicz, E., Mohammed, M., Niedźwiecki, Sz., Pawlik-Niedźwiecka, M., Raczyński, L., Rudy, Z., Silarski, M., Wiczorek, A., Wiślicki, W., Zieliński, M.: Potential of the J-PET detector for studies of discrete symmetries in decays of positronium atom — a purely leptonic system. *Acta Phys. Pol. B* **47**(2), 509 (2016) <https://doi.org/10.5506/APhysPolB.47.509>
- [26] Moskal, P., Gajos, A., Mohammed, M., Chhokar, J., Chug, N., Curceanu, C., Czerwiński, E., Dadgar, M., Dulski, K., Gorgol, M., Goworek, J., Hiesmayr, B.C., Jasińska, B., Kacprzak, K., Kapłon, Ł., Karimi, H., Kisielewska, D., Klimaszewski, K., Korcyl, G., Kowalski, P., Krawczyk, N., Krzemień, W., Kozik, T., Kubicz, E., Niedźwiecki, S., Parzych, S., Pawlik-Niedźwiecka, M., Raczyński, L., Raj, J., Sharma, S., Choudhary, S., Shopa, R.Y., Sienkiewicz, A., Silarski, M., Skurzok, M., Stępień, E.Ł., Tayefi, F., Wiślicki, W.: Testing CPT symmetry in ortho-positronium decays with positronium annihilation tomography. *Nat Commun* **12**(1), 5658 (2021) <https://doi.org/10.1038/s41467-021-25905-9>
- [27] Moskal, P., Czerwiński, E., Raj, J., Bass, S.D., Beyene, E.Y., Chug, N., Cousat, A., Curceanu, C., Dadgar, M., Das, M., Dulski, K., Gajos, A., Gorgol, M.,

- Hiesmayr, B.C., Jasińska, B., Kacprzak, K., Kaplanoglu, T., Kapłon, Ł., Klimaszewski, K., Konieczka, P., Korcyl, G., Kozik, T., Krzemień, W., Kumar, D., Moyo, S., Mryka, W., Niedźwiecki, S., Parzych, S., Del Río, E.P., Raczyński, L., Sharma, S., Choudhary, S., Shopa, R.Y., Silarski, M., Skurzok, M., Stepień, E.Ł., Tanty, P., Ardebili, F.T., Ardebili, K.T., Eliyan, K.V., Wiślicki, W.: Discrete symmetries tested at 10⁻⁴ precision using linear polarization of photons from positronium annihilations. *Nat Commun* **15**(1), 78 (2024) <https://doi.org/10.1038/s41467-023-44340-6>
- [28] Hiesmayr, B.C., Moskal, P.: Witnessing entanglement in Compton scattering processes via mutually unbiased bases. *Sci Rep* **9**(1), 8166 (2019) <https://doi.org/10.1038/s41598-019-44570-z>
- [29] Moskal, P., Kumar, D., Sharma, S., Beyene, E.Y., Chug, N., Coussat, A., Curceanu, C., Czerwiński, E., Das, M., Dulski, K., Gorgol, M., Jasińska, B., Kacprzak, K., Kaplanoglu, T., Kapłon, Ł., Klimaszewski, K., Kozik, T., Lisowski, E., Lisowski, F., Mryka, W., Niedźwiecki, S., Parzych, S., del Rio, E.P., Raczynski, L., Radler, M., Shopa, R.Y., Skurzok, M., Stepień, E.Ł., Tanty, P., Ardebili, K.T., Eliyan, K.V., Wislicki, W.: Non-Maximal Entanglement of Photons from Positron-Electron Annihilation Demonstrated Using a Novel Plastic PET Scanner. *arXiv* (2024). <https://doi.org/10.48550/ARXIV.2407.08574>
- [30] Baran, J., Borys, D., Brzeziński, K., Gajewski, J., Silarski, M., Chug, N., Coussat, A., Czerwiński, E., Dadgar, M., Dulski, K., Eliyan, K.V., Gajos, A., Kacprzak, K., Kapłon, Ł., Klimaszewski, K., Konieczka, P., Kopeć, R., Korcyl, G., Kozik, T., Krzemień, W., Kumar, D., Lomax, A.J., McNamara, K., Niedźwiecki, S., Olko, P., Panek, D., Parzych, S., Perez Del Rio, E., Raczyński, L., Simbarashe, M., Sharma, S., Shivani, Shopa, R.Y., Skóra, T., Skurzok, M., Stasica, P., Stepień, E.Ł., Tayefi, K., Tayefi, F., Weber, D.C., Winterhalter, C., Wiślicki, W., Moskal, P., Ruciński, A.: Feasibility of the J-PET to monitor the range of therapeutic proton beams. *Physica Medica* **118**, 103301 (2024) <https://doi.org/10.1016/j.ejmp.2024.103301>
- [31] Brzeziński, K., Baran, J., Borys, D., Gajewski, J., Chug, N., Coussat, A., Czerwiński, E., Dadgar, M., Dulski, K., Eliyan, K.V., Gajos, A., Kacprzak, K., Kapłon, Ł., Klimaszewski, K., Konieczka, P., Kopeć, R., Korcyl, G., Kozik, T., Krzemień, W., Kumar, D., Lomax, A.J., McNamara, K., Niedźwiecki, S., Olko, P., Panek, D., Parzych, S., Perez Del Rio, E., Raczyński, L., Sharma, S., Shivani, Shopa, R.Y., Skóra, T., Skurzok, M., Stasica, P., Stepień, E.Ł., Tayefi, K., Tayefi, F., Weber, D.C., Winterhalter, C., Wiślicki, W., Moskal, P., Ruciński, A.: Detection of range shifts in proton beam therapy using the J-PET scanner: A patient simulation study. *Phys. Med. Biol.* **68**(14), 145016 (2023) <https://doi.org/10.1088/1361-6560/acdd4c>
- [32] Moskal, P., Dulski, K., Chug, N., Curceanu, C., Czerwiński, E., Dadgar, M., Gajewski, J., Gajos, A., Grudzień, G., Hiesmayr, B.C., Kacprzak, K., Kapłon, Ł., Karimi, H., Klimaszewski, K., Korcyl, G., Kowalski, P., Kozik, T., Krawczyk,

- N., Krzemień, W., Kubicz, E., Małczak, P., Niedźwiecki, S., Pawlik-Niedźwiecka, M., Pędziwiatr, M., Raczyński, L., Raj, J., Ruciński, A., Sharma, S., Shivani, Shopa, R.Y., Silarski, M., Skurzok, M., Stępień, E.Ł., Szczepanek, M., Tayefi, F., Wiślicki, W.: Positronium imaging with the novel multiphoton PET scanner. *Sci. Adv.* **7**(42), 4394 (2021) <https://doi.org/10.1126/sciadv.abh4394>
- [33] Moskal, P., Baran, J., Bass, S., Choiński, J., Chug, N., Curceanu, C., Czerwiński, E., Dadgar, M., Das, M., Dulski, K., Eliyan, K.V., Fronczewska, K., Gajos, A., Kacprzak, K., Kajetanowicz, M., Kaplanoglu, T., Kapłon, Ł., Klimaszewski, K., Kobylecka, M., Korcyl, G., Kozik, T., Krzemień, W., Kubat, K., Kumar, D., Kunikowska, J., Mączewska, J., Migdał, W., Moskal, G., Mryka, W., Niedźwiecki, S., Parzych, S., Perez Del Rio, E., Raczyński, L., Sharma, S., Shivani, Shopa, R.Y., Silarski, M., Skurzok, M., Tayefi, F., Tayefi, K., Tanty, P., Wiślicki, W., Królicki, L., Stępień, E.Ł.: First Positronium Image of the Human Brain *in Vivo* (2024). <https://doi.org/10.1101/2024.02.01.23299028>
- [34] Moskal, P., Stępień, E.Ł.: Prospects and clinical perspectives of total-body PET imaging using plastic scintillators. *PET Clinics* **15**(4), 439–452 (2020) <https://doi.org/10.1016/j.cpet.2020.06.009>
- [35] Baran, J., Krzemien, W., Raczyński, L., Bała, M., Coussat, A., Parzych, S., Chug, N., Czerwiński, E., Curceanu, C.O., Dadgar, M., Dulski, K., Eliyan, K., Gajewski, J., Gajos, A., Hiesmayr, B., Kacprzak, K., Kapłon, Ł., Klimaszewski, K., Korcyl, G., Kozik, T., Kumar, D., Niedźwiecki, S., Panek, D., del Rio, E.P., Ruciński, A., Sharma, S., Shivani, Shopa, R.Y., Skurzok, M., Stępień, E., Tayefiardebili, F., Tayefiardebili, K., Wiślicki, W., Moskal, P.: Realistic Total-Body J-PET Geometry Optimization – Monte Carlo Study. *arXiv* (2022). <https://doi.org/10.48550/ARXIV.2212.02285>
- [36] Shopa, R.Y., Baran, J., Klimaszewski, K., Krzemień, W., Raczyński, L., Wiślicki, W., Brzeziński, K., Chug, N., Coussat, A., Curceanu, C., Czerwiński, E., Dadgar, M., Dulski, K., Gajewski, J., Gajos, A., Hiesmayr, B.C., Valsan, E.K., Korcyl, G., Kozik, T., Kumar, D., Kapłon, Ł., Moskal, G., Niedźwiecki, S., Panek, D., Parzych, S., Rio, E.P.D., Ruciński, A., Sharma, S., Shivani, S., Silarski, M., Skurzok, M., Stępień, E., Ardebili, F.T., Ardebili, K.T., Moskal, P.: TOF MLEM adaptation for the total-body J-PET with a realistic analytical system response matrix. *IEEE Trans. Radiat. Plasma Med. Sci.* **7**(5), 509–520 (2023) <https://doi.org/10.1109/TRPMS.2023.3243735>
- [37] Shepp, L.A., Vardi, Y.: Maximum likelihood reconstruction for emission tomography. *IEEE Transactions on Medical Imaging* (2) (1982)
- [38] Pépin, A., Stute, S., Jan, S., Comtat, C.: Normalization of monte carlo PET data using GATE. In: 2011 IEEE Nuclear Science Symposium Conference Record, pp. 4196–4200. IEEE, Valencia, Spain (2011). <https://doi.org/10.1109/NSSMIC.2011.6153804>

- [39] Sarrut, D., Bała, M., Bardiès, M., Bert, J., Chauvin, M., Chatzipapas, K., Dupont, M., Etxebeste, A., M Fanchon, L., Jan, S., Kayal, G., S Kirov, A., Kowalski, P., Krzemien, W., Labour, J., Lenz, M., Loudos, G., Mehadji, B., Ménard, L., Morel, C., Papadimitroulas, P., Rafecas, M., Salvadori, J., Seiter, D., Stockhoff, M., Testa, E., Trigila, C., Pietrzyk, U., Vandenberghe, S., Verdier, M.-A., Visvikis, D., Ziemons, K., Zvolský, M., Roncali, E.: Advanced monte carlo simulations of emission tomography imaging systems with GATE. *Phys. Med. Biol.* **66**(10), 10–03 (2021) <https://doi.org/10.1088/1361-6560/abf276>
- [40] Moskal, P., Niedźwiecki, Sz., Bednarski, T., Czerwiński, E., Kapłon, Ł., Kubicz, E., Moskal, I., Pawlik-Niedźwiecka, M., Sharma, N.G., Silarski, M., Zieliński, M., Zoń, N., Białas, P., Gajos, A., Kochanowski, A., Korcyl, G., Kowal, J., Kowalski, P., Kozik, T., Krzemień, W., Molenda, M., Pałka, M., Raczyński, L., Rudy, Z., Salabura, P., Słomski, A., Smyrski, J., Strzelecki, A., Wieczorek, A., Wiślicki, W.: Test of a single module of the J-PET scanner based on plastic scintillators. *Nuclear Instruments and Methods in Physics Research Section A: Accelerators, Spectrometers, Detectors and Associated Equipment* **764**, 317–321 (2014) <https://doi.org/10.1016/j.nima.2014.07.052>
- [41] Merlin, T., Stute, S., Benoit, D., Bert, J., Carlier, T., Comtat, C., Filipovic, M., Lamare, F., Visvikis, D.: CASToR: A generic data organization and processing code framework for multi-modal and multi-dimensional tomographic reconstruction. *Phys. Med. Biol.* **63**(18), 185005 (2018) <https://doi.org/10.1088/1361-6560/aadacl>
- [42] Jacobs, F., Sundermann, E., De Sutter, B., Christiaens, M., Lemahieu, I.: A fast algorithm to calculate the exact radiological path through a pixel or voxel space. *Journal of computing and information technology* **6**(1), 89–94 (1998)
- [43] Dai, B., Daube-Witherspoon, M.E., McDonald, S., Werner, M.E., Parma, M.J., Geagan, M.J., Viswanath, V., Karp, J.S.: Performance evaluation of the PennPET explorer with expanded axial coverage. *Phys. Med. Biol.* **68**(9), 095007 (2023) <https://doi.org/10.1088/1361-6560/acc722>
- [44] Cherry, S.R., Dahlbom, M.: PET: Physics, instrumentation, and scanners. In: Phelps, M.E. (ed.) *PET*, pp. 1–117. Springer, New York, NY (2006). https://doi.org/10.1007/0-387-34946-4_1
- [45] Siddon, R.L.: Fast calculation of the exact radiological path for a three-dimensional CT array. *Medical Physics* **12**(2), 252–255 (1985) <https://doi.org/10.1118/1.595715>